Laser-driven tunneling photocurrent as a source of midinfrared to microwave multidecade supercontinua yoked to high-order harmonics

A. A. Voronin and A. M. Zheltikov

Phys. Rev. A **101**, 043813 — Published 13 April 2020

DOI: 10.1103/PhysRevA.101.043813

Laser-driven tunneling photocurrent as a source of high-harmonic-yoked mid-infrared-to-microwave multidecade supercontinua

A.A. Voronin[1,2] and A.M. Zheltikov[1,2,3*]

[1] Physics Department, International Laser Center, M.V. Lomonosov Moscow State University, Moscow 119992, Russia

[2] Russian Quantum Center, ul. Novaya 100, Skolkovo, Moscow Region, 143025 Russia

[3] Department of Physics and Astronomy, Texas A&M University, College Station TX 77843, USA

[*] Corresponding author: zheltikov@physics.msu.ru

Electron tunneling induced by a strong-field laser driver can lead to an ultrafast stepwise buildup of the photoelectron density ρ. When the laser field is strong enough, each such step in the temporal profile of ρ is confined well within the field cycle, providing an ultrabroadband, multidecade force that drives the photoelectron current j. However, whether or not the photocurrent can emit electromagnetic radiation with such an extraordinarily broad spectrum depends on the damping, which defines the low-frequency cutoff in the spectrum of this radiation. We show that, with a suitable choice of the gas pressure and parameters of the laser driver, the laser-induced tunneling photocurrent can serve as a source of a remarkably broadband electromagnetic radiation with a multidecade spectrum stretching from the vacuum ultraviolet all the way down to the microwave range. We demonstrate that the supercontinuum fields emitted by individual photocurrent steps, induced by different field half-cycles, can coherently combine, giving rise to well-resolved high-order harmonics on the high-frequency end of the spectrum yoked to a bright mid-infrared-to-microwave supercontinuum, dominating the long-wavelength part of the multidecade radiation output.

I. INTRODUCTION

Laser-induced electron tunneling is one of the central effects in strong-field optical physics, which brings quantum weirdness to ultrafast optical science [1 – 7] and which plays a prominent

role in a remarkable variety of nonlinear-optical scenarios, sometimes as diverse as high-order harmonic generation [8], laser filamentation [9, 10], and optical breakdown in gases and solids [11]. In a canonical picture of tunneling photoionization [12, 13], a strong laser field periodically modulates the potential that binds electrons in atoms, molecules, or sites of a crystal lattice, facilitating the tunneling of electrons through the resulting nonstationary potential barrier, with the maximum tunneling probability achieved near the maxima of the driver field [14, 15]. Photoelectron dynamics behind the barrier can often be described semiclassically [16, 17]. Once they have exited the potential barrier, the photoelectrons are accelerated by the laser field, gaining a kinetic energy. Electrons on suitable trajectories are driven back by the laser field to recollide and recombine with their parent ions or holes they have left behind [16]. Due to the strong nonlinearity of the potential that they overcome in this process, these electrons emit high-order harmonics. This strong-field laser–matter interaction scenario is at the heart of rapidly growing attosecond technologies [8].

Other photoelectrons are on nonrecolliding trajectories. In the same semiclassical framework, supported by quantum-mechanical analysis [18, 19], the optical response of such electrons can be described in terms of the photoelectron current, $j(t) = \int_{-\infty}^{t} ev(t', t)\,(\partial\rho/\partial t\,|_{t=t'})dt'$, where e is the electron charge, $v(t', t)$ is the velocity of photoelectrons undergoing ionization at the instant of time t', and $d\rho(t') = (\partial\rho/\partial t\,|_{t=t'})dt'$ is the photoelectron density produced by the laser field within the time interval from t' to $t' + dt$. Laser-induced tunneling gives rise to a rapid, almost stepwise buildup of the electron density $\rho(t)$, leading to an ultrafast modulation of the photoelectron current $j(t)$. Since these ionization steps in $\rho(t)$ are tightly locked to the maxima of the driver field, they recur every field half-cycle, making the photocurrent $j(t)$ a source of odd-order harmonics [20], which can be detected via direct photoionization-yield measurements [21], as well as by all-optical means, using high-harmonic-generation spectroscopy [22, 23].

In a two-color field, consisting of, e.g., a laser pulse with a central frequency ω_0 and its second harmonic, the temporal symmetry of the laser driver can be removed with an appropriate phase shift of one field with respect to the other [24 – 26]. In such a setting, the prohibition on even-order nonlinear processes is lifted, and the generation of low-frequency electromagnetic fields with central frequencies ranging from ≈ 0.1 to ≈ 50 THz becomes possible via $2\omega_0 - \omega_0 -$

ω_0 four-wave mixing (FWM) [27 – 31] or due to photoionization-current radiation [25, 26, 32 – 37].

As laser-based THz sources find increasing applications in molecular spectroscopy, bioimaging, and security scanning [38], the question as to whether or not optical methods of frequency down-conversion can be extended beyond the THz range, to enable millimeter-wave (MMW) or even microwave generation, remains open. As an important finding, the spectrum of conical emission from laser filaments has been shown to extend to the gigahertz (GHz) and even sub-GHz range [39, 40], suggesting a way toward a laser source of GHz and sub-GHz radiation, which would help avoid strong atmospheric absorption bands in the THz range, thus facilitating remote sensing applications. Moreover, progress in this area would pave the ways toward the integration of ultrafast photonics with rapidly growing MMW and microwave technologies [41 – 43], thus opening new avenues in radio astronomy, remote sensing, telecommunication, medical imaging, and security screening [44 – 46].

Here, we show that such an integration is possible. We demonstrate below in this paper that, with a suitable choice of the gas pressure and parameters of the laser driver, the laser-induced tunneling photocurrent can provide a source of a remarkably broadband electromagnetic radiation with a multidecade spectrum stretching from the vacuum ultraviolet all the way down to the microwave range. We will show that the supercontinuum fields emitted by individual photocurrent steps, induced by different field half-cycles, can coherently combine, giving rise to well-resolved high-order harmonics on the high-frequency end of the spectrum along with a bright mid-infrared-to-microwave supercontinuum, dominating the long-wavelength part of the multidecade radiation output.

II. MODEL

A. Photoelectron current and radiation field

Our analysis of the photoelectron current as a source of low-frequency radiation is based on a standard semiclassical equation [9, 10, 47]

$$\partial j(\eta)/\partial\eta + \nu_e j(\eta) = (e^2/m_e)\rho(\eta)E(\eta), \quad (1)$$

where η is the time in the retarded frame of reference, $E(\eta)$ is the driver field, ν_e is the damping rate, e is the electron charge, and m_e is the electron mass.

The electric field radiated by the photoelectron current $j(x', y', z', \eta)$ localized within a volume ΔV can be expressed in the form of the diffraction integral [48, 49],

$$E_j(x,y,z,\eta) = -\frac{1}{4\pi\varepsilon_0}\iiint_{\Delta V}\left(\frac{1}{c^2 R}\frac{\partial j(x',y',z',\eta)}{\partial \eta}\right)dx'\,dy'\,dz',$$

where c is the speed of light in vacuum, ε_0 is the vacuum permittivity, $R^2 = [(x'-x)^2 + (y'-x)^2 + (z'-x)^2]^{1/2}$, and x, y, z are the spatial coordinates of the point of observation.

In the far field, $R^2 >> (x')^2 + (y')^2 + (z')^2$, i.e., at large distances from ΔV, such that the spatial coordinates x', y', z' within ΔV are no longer resolved, with $j(\eta) \approx j(x', y', z', \eta)$, this integral reduces to $E_j(\eta) \approx -\Delta V(4\pi\varepsilon_0 c^2 R)^{-1}[\partial j(\eta)/\partial\eta]$, leading to a widely accepted relation [9, 10]

$$E_j(\eta) \propto \partial j(\eta)/\partial\eta. \quad (2)$$

The field intensity is then found as $I_0 = c\varepsilon_0 n_0 \max([E(\eta)]^2)$, where n_0 is the refractive index and $\max([E(\eta)]^2)$ stands for the maximum of $[E(\eta)]^2$ within the pulse.

The Fourier transform of Eq. (2) leads to the spectrum of $E_j(\eta)$ in the form $E_j(\omega) \propto \omega j(\omega)$, where $j(\omega)$ is the Fourier transform of the time-dependent photocurrent $j(\eta)$,

$$j(\omega) = e^2\,[m_e(\omega^2 + \nu_e^2)]^{-1}(i\omega + \nu_e)\int_{-\infty}^{\infty}\rho(\eta)E(\eta)e^{-i\omega\eta}d\eta. \quad (3)$$

The model of broadband radiation by a field-driven photocurrent as defined by Eqs. (1) – (3) does not include any propagation effects. However, the radiation source term in this model, $\partial j(\eta)/\partial\eta$, is consistent with a canonical picture of diffraction in the far field [48] and helps reproduce important signatures of far-field diffraction. Indeed, the Fourier transform of the field radiated by $j(\eta)$, as defined by Eq. (2), leads to an intensity spectrum $|E_j(\omega)|^2 \propto |\omega j(\omega)|^2$ with a signature ω^2 factor, typical of far-field radiation spectra [49]. That $|E_j(\omega)|^2$ decreases toward lower frequencies and vanishes at $\omega = 0$ is consistent with dc-field no-propagation – another signature result of diffraction theory.

B. Field-induced and impact ionization

The electron density $\rho(\eta)$ entering the broadband driver term in Eq. (1) is generally a sum, $\rho(\eta) = \rho_\gamma(\eta) + \rho_\sigma(\eta)$, of electron densities $\rho_\gamma(\eta)$ and $\rho_\sigma(\eta)$ produced, respectively, via photoionization and impact ionization [9, 10]. The ratio

$$\Sigma = \int_{-\infty}^{\infty} d\eta\rho_\sigma(\eta)/\int_{-\infty}^{\infty} d\eta\rho_\gamma(\eta) \quad (4)$$

is a function of the gas pressure, sort of the gas, and parameters of laser radiation.

A standard treatment of photoionization leads to

$$d\rho_\gamma(\eta)/d\eta = w(\eta)[\rho_0 - \rho_\gamma(\eta)]. \quad (5)$$

Here, ρ_0 is the density of neutral species undergoing photionization and the tunneling rate $w(\eta)$ is calculated using the quasistatic-approximation Ammosov–Delone–Krainov-type equation [9, 50],

$$w(\eta) = \omega_a|C_{n',l'}|^2\,[U_0/(2Ry)]\,[(2E_0)/|E(\eta)|]^{\alpha}\exp[-(2/3)\,E_0/|E(\eta)|], \quad (6)$$

where $\omega_a \approx 4.13\cdot10^{16}$ Hz is the atomic unit of frequency, $E_0 = E_a(U_0/Ry)^{3/2}$, $E_a \approx 5.14\cdot10^{11}$ V/m is the atomic field, U_0 is the ionization potential, Ry is the Rydberg constant, $\alpha = 2n' - 3/2$, $|C_{n',l'}|^2 = 2^{2n'}\,[n'\,\Gamma(n' + l' + 1)\,\Gamma(n' - l')]^{-1}$, $n' = n - \delta l$, $l' = l - \delta l$, $\delta l = n - (U_0/Ry)^{-1/2}$, $n' = n - \delta l$, $l' = l - \delta l$, $\delta l = n - (Ry/U_0)^{1/2}$, n is the principal quantum number, and l is the orbital quantum number.

With a canonical model of impact ionization [9, 10],

$$d\rho_\sigma(\eta)/d\eta = (\sigma/U_i)\rho(\eta)I(\eta), \quad (7)$$

where $\sigma = e^2\tau_e[m_e\varepsilon_0 n_0 c(1 + \omega^2\tau_e^2)]^{-1}$, $U_i = U_0 + U_p$, U_p is the electron pondermotive energy, $\tau_e = 1/\nu_e$ is the collision time, and $I(\eta) = c\varepsilon_0 n_0[E(\eta)]^2$ is the instantaneous field intensity.

With atmospheric air at a variable pressure p chosen as a gas target, we take $U_0 = 12.1$ eV, $n = 2$, $l = 0$, and $\rho_0 = 5.6\cdot10^{18}(p/p_{atm})$ cm^{-3} [9], p_{atm} being the atmospheric pressure. The collision time τ_e is calculated using a standard approximation [9]

$$\tau_e = 350(p_{atm}/p) \text{ fs}. \quad (8)$$

The laser field is taken in the form

$$E(\eta) = E_0[\exp(-\eta^2/\tau_p^2)\cos(i\omega_0\eta) + \xi\exp(-\eta^2/\tau_p^2)\cos(2i\omega_0\eta + \theta)], \quad (9)$$

where $\tau_p^2 = 0.64\tau_0^2$, τ_0 is the FWHM pulse width, and θ is the relative phase.

In Fig. 1a, we plot the ratio Σ calculated as a function of the gas pressure p and the radiation wavelength λ_0 for $I_0 = 200$ TW/cm^2, $\theta = \pi/2$, and $\xi = 0.3$. As a general tendency, the relative significance of impact ionization monotonically grows with p and λ_0. In the high-p long-λ_0 regime, impact ionization will thus dominate the buildup of the electron density [51, 52], setting a limit, in p and λ_0, on ultrafast optical phenomena related to photoionization, including broadband radiation by photoelectron currents. In view of this limitation, we set the driver wavelength in our calculations at $\lambda_0 = 800$ nm and vary the gas pressure within the range from ~ 1 mbar to 1 bar. In this range of parameters, $\Sigma < 2\%$ (Fig. 1a). With impact ionization effects being negligible in the studied parameter space, we set $\rho(t) = \rho_\gamma(t)$ in all calculations below.

Integrating Eq. (5) with the photoionization rate as defined by Eq. (6), the field in the form (9), and $\rho_0 = 5.6\cdot10^{18}(p/p_{atm})$ cm^{-3} for atmospheric air at $p = 1$ mbar, we find $\rho \approx 10^{15}$ cm^{-3}. With an electron temperature $T_e \approx 1 - 10$ eV, this gives a Debye length $\lambda_D \approx 0.3 - 1$ μm. The number of particles within the Debye sphere is then estimated as $\rho(\lambda_D)^3 \approx 30 - 1000$, satisfying the condition of plasma quasi-neutrality. Photoelectrons will thus interact with a screened potential, rather than with the Coulomb potential of individual ion cores, even at the lowest-bound pressure from the studied pressure range.

C. Collision damping in the low-pressure limit

Collision damping is included as a separate term in Eq. (1) for the dynamics of the photoelectron current, translating into a ν_e-dependent term in Eq. (2) for the spectrum of the photocurrent and, hence, for the spectrum of radiation. As will be shown below, the collision damping of the field-driven photocurrent dynamics defines, along with the duration of photoionization steps in $j(\eta)$, the low-frequency cutoff in photocurrent radiation spectra.

Given the importance of the collision damping for the properties of broadband radiation generated by photocurrents, it would be meaningful to examine the validity range of the commonly accepted approximation of Eq. (8) for the collision rate, paying a particular attention to the behavior of ν_e as a function of the gas pressure in the range of low p. With this goal in mind, we represent the collision rate as a sum [53]

$$\nu_e = \nu_{eO} + \nu_{eN} + \nu_{ei}, \tag{10}$$

where ν_{eO} and ν_{eN} are the rates of electron collisions with, respectively, O_2 and N_2 molecules in air, and ν_{ei} is the rate of electron–ion collisions, dominated in the considered range of parameters by electron collisions with oxygen ions.

The rates of electron–neutral collisions are estimated as [53, 54]

$$\nu_{eO} = (\rho_O - \rho)\, \xi_O(W_e)\, (W_e/m_e)^{1/2}, \tag{11}$$

$$\nu_{eN} = \rho_N \xi_N(W_e)\, (W_e/m_e)^{1/2}, \tag{12}$$

where $\rho_O = 5.4\cdot10^{18}(p/p_{atm})$ and $\rho_N = 2.2\cdot10^{19}(p/p_{atm})$ are the densities of O_2 and N_2 molecules, respectively, $\xi_O(W_e)$ and $\xi_N(W_e)$ are the cross sections of electron collisions with O_2 and N_2 molecules, respectively, and W_e is the electron kinetic energy.

The electron–ion collision rate is given by [53, 55]

$$\nu_{ei} \approx 2.9\cdot10^{-6} \rho\, \lambda_{ei}(W_e)^{-3/2}, \tag{13}$$

where ρ is in cm^{-3} , W_e is in eV, and λ_{ei} is the Coulomb integral.

The electron kinetic energy W_e enters into Eqs. (11) – (13) as an important parameter that has a significant effect on both electron–neutral and electron–ion collision rates. This parameter can be estimated from the drift velocity of photoelectrons [25]:

$$\upsilon_d = (eE_0/(m_e\omega_0))\cdot\sin\varphi + (e\xi E_0/(2m_e\omega_0))\cdot\sin(2\varphi + \theta), \quad (14)$$

where $\varphi = \omega_0 t_e$ and t_e is the instant of time when the electron undergoes photoionization.

Setting $\theta = \pi/2$ for the maximum yield of the low-frequency part of supercontinuum radiation [25], we arrive at

$$\upsilon_m = e/(m_e\omega_0)\,(E_0 + \xi E_0/2). \quad (15)$$

With $\lambda_0 = 800$ nm, $E_0 = 3\cdot10^8$ V/cm, and $\xi = 0.3$, Eq. (15) yields the mean electron kinetic energy $W_e \approx 9$ eV. The cross sections of electron–neutral collisions for this electron kinetic energy are, according to the reference data [56], $\xi_O(W_e = 9\text{ eV}) \approx 5\cdot10^{-16}$ cm^2 and $\xi_N(W_e = 9\text{ eV}) \approx 8\cdot10^{-16}$ cm^2.

We then integrate Eq. (5) with the photoionization rate as defined by Eq. (6), the field in the form (9), and $\rho_O = 5.4\cdot10^{18}(p/p_{atm})$ cm^{-3} and $\rho_N = 2.2\cdot10^{19}(p/p_{atm})$ cm^{-3} for atmospheric air at $p = 1$ bar to find $\rho \approx 10^{18}$ cm^{-1}. We now have all the ammunition to estimate the electron–neutral and electron–ion collision rates as defined by Eqs. (11) – (13): $\nu_{eO} \approx 0.34$ THz, $\nu_{eN} \approx 1.9$ THz, and $\nu_{ei} \approx 0.6$ THz. The electron collision time is then estimated as $\tau_e = 1/\nu_e \approx 1/(\nu_{eO} + \nu_{eN} + \nu_{ei}) \approx$ 350 fs. This result is comforting indeed as it is in full agreement with a standard, commonly accepted estimate for τ_e in atmospheric air at $p = 1$ bar as given by Eq. (8).

With this important check successfully passed, we can go back and inspect the pressure scaling of the collision rates ν_{eO}, ν_{eN}, and ν_{ei}. Eqs. (11) and (12) are seen to predict a linear scaling of the electron–neutral collision rates ν_{eO} and ν_{eN} with the gas pressure p. Within the range of gas pressures studied here, this prediction is consistent with the available data (see, e.g., Refs. 53, 56 – 58). The pressure dependence of the electron–ion collision rate is, however, much more complicated. Indeed, even in an elementary approximation as described by Eq. (13), the electron–ion collision rate is a product of two pressure-dependent factors – the electron density and the Coulomb integral. For $W_e < 10$ eV, that is, for the range of electron energies relevant to photocurrent-driven broadband radiation generation, a standard estimate on λ_{ei} reads [53, 55]

$$\lambda_{ei} \approx 23 - \ln[(\rho)^{1/2}(W_e)^{-3/2}]. \quad (16)$$

Repeating the above-described routine of collision-rate calculations, this time for p = 1 mbar, we find $\nu_{eO} \approx 0.34$ GHz, $\nu_{eN} \approx 1.9$ GHz, and $\nu_{ei} \approx 0.97$ GHz. The electron–neutral collision rates are now $p_{atm}/p = 10^3$ times lower, as expected. The electron–ion collision rate, however, is only ≈ 620 times lower in a noticeable disagreement with the prediction of Eq. (8). Moreover, this collision rate is of the same order of magnitude as the sum of the electron–neutral collision rates, $\nu_{eO} + \nu_{eN} \approx 2.2$ GHz. The electron collision time is then estimated as $\tau_e \approx 1/(\nu_{eO} + \nu_{eN} + \nu_{ei}) \approx 310$ ps. We see that, within the range of p from 1 mbar to 1 bar, the pressure dependence of the Coulomb logarithm gives rise to a maximum error of ≈ 11% in τ_e calculations relative to predictions of Eq. (8) with its approximation of p_{atm}/p scaling. While such an error can certainly be tolerated for approximate, order-of-magnitude analysis, we still choose to use a more accurate approximation provided by Eqs. (10) – (14) and (16) in our ν_e calculations and in our analysis through the rest of this paper.

III. RESULTS AND DISCUSSION

A. Photoelectron current as a driver of multidecade radiation

Electron tunneling induced by a strong-field laser driver gives rise to signature steps in the buildup of the electron density $\rho(\eta)$ [Fig. 1(b)], with each step locked to the field maximum within the respective field half-cycle [Figs. 2(a) – 2(c)]. The electron tunneling rate $w(\eta)$, in accordance with Eq. (3), rapidly increases with the growth in I_0, giving rise to steeper ionization steps in the temporal profile of the photoelectron current $\rho(\eta)$ [Figs. 2(a) – 2(c)]. Specifically, for $I_0 \approx 200$ TW/cm^2, a typical step duration, δt, becomes less than 0.5 fs for the chosen parameters of the field [Fig. 1(b)].

With each ionization step confined well within the field cycle [Fig. 1(b)], $\rho(\eta)$ provides an ultrabroadband, multidecade force $F(\eta) = (e^2/m_e)\rho(\eta)E(\eta)$, which drives, in accordance with Eq. (1), the photoelectron current $j(\eta)$. A finite photocurrent damping rate ν_e, on the other hand, leads to an exponential decay of $j(\eta)$ on a time scale τ_e [Fig. 1(c)] limiting the bandwidth of radiation emitted by $j(\eta)$ and dictating, as can be seen from Eq. (3), a low-frequency cutoff, $\omega_c \approx \nu_e$, in the spectrum of this radiation [dotted vertical lines in Figs. 1(d) and 2(d)]. While collisions damp the photocurrent dynamics driven by the laser field, defining, along with the duration of photoionization steps in $j(\eta)$, the low-frequency cutoff in photocurrent radiation spectra, the asymptotic behavior of photocurrent radiation spectra $j(\omega)$ at very low frequencies, below this

low-frequency cutoff, i.e., for $\omega << \nu_e$, follows the ω^2 scaling regardless of the collision rate. Indeed, as perhaps best seen in Fig. 3b, for $\omega << \nu_e$, all the $|E_j(\omega)|^2$ spectra converge to a ω^2 asymptote.

In a laser field consisting of $M/2$ cycles, radiation fields emitted by individual photocurrent steps coherently combine, giving rise to a signature interference pattern [47], $\Phi(M, \omega/\omega_0) = [\sin(M\pi\omega/\omega_0)/\sin(\pi\omega/\omega_0)]^2$. The main maxima of this interference pattern occur at frequencies $\omega_l = l\omega_0$, $l = 0, 1, 2, ...$, and have a spectral width of $\delta\omega \approx \omega_0/M \approx \pi/\tau_0 \approx \Delta\omega$, where $\Delta\omega$ is the bandwidth of the laser driver. On the high-frequency side of the radiation spectrum, these maxima of $\Phi(M, \omega/\omega_0)$ show up as peaks at harmonic frequencies $\omega_l = l\omega_0$ with $l \geq 2$ [Fig. 2(d)]. As the driver pulse width τ_0 increases, leading to an increase in the number of field half-cycles generating ionization steps in $\rho(\eta)$, the $\omega_{l \geq 2} = l\omega_0$ harmonic peaks become better resolved as their spectral width decreases as $1/\tau_0$ [Fig. 2(d)].

The lowest frequencies in the spectrum of the driving force $F(\eta) = (e^2/m_e)\rho(\eta)E(\eta)$ are suppressed by electron–ion and electron–neutral collisions, leading to an exponential decay of the photocurrent $j(\eta)$ on a time scale τ_e [Fig. 1(c)]. To quantify the filtering ability of these collisions, included into our model via the phenomenological damping term $\nu_e j(\eta)$ in Eq. (1), we focus on the low-frequency, $\omega/(2\pi) \leq 100$ THz part of the $|E_j(\omega)|^2$ spectra generated by a two-color laser field (9) in atmospheric air. These spectra, shown in Figs. 2(d), 3(a), and 3(b), display a well-defined low-frequency cutoff, at $\omega_c \approx \nu_e$, and, perhaps less clearly resolved, yet definable maximum $|E_{max}|^2$ at the frequency ω_m, such that $|E_j(\omega_m)|^2 = |E_{max}|^2$ for $\omega/2\pi \leq 100$ THz. Filled circles in Fig. 3c show this frequency ω_m for the numerically simulated $|E_j(\omega)|^2$ spectra in Figs. 2d, 3a, 3b plotted as a function of the gas pressure p. As a clear tendency, ω_m shifts toward lower frequencies at lower p.

This behavior of $|E_j(\omega)|^2$ is readily understood in terms of the pressure dependence of the electron collision time ν_e. Lower gas pressures correspond to longer τ_e and, hence, lower ν_e in Eq. (3), thus red-shifting the maxima and the cutoff frequencies in $|E_j(\omega)|^2$ and allowing the supercontinua radiated by $j(\eta)$ to be extended to lower frequencies. Specifically, at $p = 1$ mbar, the low-frequency cutoff is shifted, as can be seen from Figs. 2(d) and 3(b), to frequencies as low as a few gigahertz. In this regime, the photocurrent $j(\eta)$ provides a source of broadband radiation with high-order harmonics on the high-frequency end of its spectrum yoked to a bright mid-IR-

to-microwave supercontinuum, dominating the long-wavelength part of the multidecade radiation output [Fig. 2(d)].

B. Multidecade supercontinua and their properties

1. Low-frequency cutoff

To gain deeper insights into the physics behind the properties of such supercontinua, we employ the following naïve approximation for the long-wavelength part of the supercontinuum radiated by the tunneling photocurrent [47]:

$$|E_j(\omega)|^2 \propto \omega^2/(\omega^2 + \nu_e^2)\exp(-\omega^2/\sigma^2), \quad (17)$$

where σ is the bandwidth of a typical tunneling peak in the ionization-rate profile $w(\eta)$.

With $\omega^2 << \nu_e^2$, Eq. (17) correctly describes the $\propto \omega^2$ scaling as a universal asymptotic behavior of $|E_j(\omega)|^2$, which is independent of the collision rate and is fully consistent with far-field diffraction analysis [48, 49]. Equating the derivative of $|E_j(\omega)|^2$ in ω to zero, we find that $|E_j(\omega)|^2$ reaches its maximum at $\omega_q \approx [(\nu_e^4/4 + \sigma^2\nu_e^2)^{1/2} - \nu_e^2/2]^{1/2}$. Since the tunneling peaks in $w(\eta)$ are extremely short and we are interested in a weak-damping regime, we take the $\nu_e^2 << \sigma^2$ limit to find $\omega_q \approx (\nu_e\sigma)^{1/2} \propto p^{1/2}$. Despite all the naivety of the arguments leading to this prediction, the $\omega_q \propto p^{1/2}$ fit [solid line in Fig. 3(c)] agrees remarkably well with the pressure dependence of the frequency ω_m in numerically simulated $|E_j(\omega)|^2$ spectra [circles in Fig. 3(c)]. Notably, this $p^{1/2}$ scaling of ω_m and ω_q is distinctly different from the pressure dependence of the long-wavelength cutoff frequency ω_c, which is defined by the collision rate ν_e and follows the pressure scaling of ν_e (see Section II.C).

2. High-frequency cutoff

When the driver pulse accommodates multiple field cycles, the long-wavelength part of $|E_j(\omega)|^2$ is seen to exhibit not only the low-frequency, but also a high-frequency cutoff [Figs. 2(d), 3(a), 3(b)]. As an important tendency, the high-frequency edge of $|E_j(\omega)|^2$ becomes sharper as the driver pulse width τ_0 increases [Figs. 2(d), 3(a), 3(b)]. These properties of $|E_j(\omega)|^2$ can be adequately explained in terms of the interference of ionization steps in the $\rho(\eta)$ profile. Indeed, as shown above, the $\Phi(M, \omega/\omega_0)$ factor dictates a high-frequency edge ω_h of the long-wavelength part of $|E_j(\omega)|^2$ at $\omega_h \approx \pi/\tau_0$.

We quantify the position of this cutoff in numerically simulated $|E_j(\omega)|^2$ spectra in terms of the frequency ω_f in the high-frequency slope of $|E_j(\omega)|^2$ such that $|E_j(\omega_f)|^2 = 0.7|E_{max}|^2$, where $|E_{max}|^2$ is the maximum of $|E_j(\omega)|^2$ within the frequency range $\omega/(2\pi) \leq 100$ THz. In Fig. 3(d), we plot the high-frequency cutoff frequency ω_f defined for numerically simulated $|E_j(\omega)|^2$ spectra [Figs. 2(d), 3(a), 3(b)] as a function of the driver pulse width τ_0. This dependence is seen to agree well with a simple $\omega_h \approx 1/\tau_0$ prediction [solid line in Fig. 3(d)]. With $\tau_0 = 10$ fs, the long-wavelength part of $|E_j(\omega)|^2$ exhibits a high-frequency cutoff at $\omega_f/(2\pi) \approx$ 50 THz [green line in Fig. 2(d)], corresponding to a wavelength of 6 μm in the mid-infrared range. With its long-wavelength cutoff at ~ 1 GHz, this supercontinuum spans over 4.7 decades, stretching from the mid-IR all the way down to the microwave range.

Notably, while the low-frequency cutoff of $|E_j(\omega)|^2$ is controlled by the gas pressure and is independent of the pulse width τ_0, the high-frequency edge of this spectrum is controlled by the driver pulse width, showing little to no sensitivity to the gas pressure. This finding suggests two independent control knobs to efficiently tune the microwave-to-mid-IR part of supercontinua emitted by ultrafast tunneling photocurrents.

C. Sources of multidecade supercontinua: photocurrent versus four-wave mixing

To better appreciate the remarkable ability of the tunneling photocurrent to generate supercontinua extending deep into the MMW-to-microwave range, it is instructive to compare the THz-to-microwave part of $|E_j(\omega)|^2$ with a generic spectrum of radiation generated by the third-order polarization via the $2\omega_0 - \omega_0 - \omega_0$ two-color FWM, $|E_p(\omega)|^2 \propto |\omega^2 \iint_0^\infty E(\omega')E(\omega'' - \omega')E(\omega - \omega' - \omega'')d\omega''d\omega'|^2$, where $E(\omega) = \int_{-\infty}^{\infty} E(\eta)e^{-i\omega\eta}d\eta$. This equation has been shown to provide an adequate approximation for the spectra of FWM-related THz signals in the scenarios where the spectral distortions due to propagation effects are weak [59]. For a two-color driver field as defined by Eq. (9) with parameters as specified above, the $E_p(\omega)$ spectrum [shown by blue shading in Figs. 3(a) and 3(b)] displays a signature peak at ≈ 15 THz. Generation of longer wavelengths in FWM is strongly suppressed by the ω^2 factor in front of the convolution integral. As a result, $|E_p(\omega)|^2$ rapidly falls off toward its low-frequency end, reaching a 0.1 level of its peak intensity already at $\nu = \omega/(2\pi) \approx 5.7$ THz and yielding virtually no signal in the MMW and microwave ranges [Figs. 3(a) and 3(b)].

IV. CONCLUSION

To summarize, we have shown that, with a suitable choice of the gas pressure and parameters of the laser driver, the laser-induced tunneling photocurrent can provide a source of a remarkably broadband electromagnetic radiation with a multidecade spectrum stretching from the vacuum ultraviolet all the way down to the microwave range. We have demonstrated that the supercontinuum fields emitted by individual photocurrent steps, induced by different field half-cycles, can coherently combine, giving rise to well-resolved high-order harmonics on the high-frequency end of the spectrum along with a bright mid-IR-to-microwave supercontinuum, dominating the long-wavelength part of the multidecade radiation output.

ACKNOWLEDGMENTS

This research was supported in part by the Russian Foundation for Basic Research (projects nos. 18-29-20031, 19-02-00473, 18-02-40034, 18-32-20196), Russian Science Foundation (project no. 17-12-01533 – ultrafast spectrochronography; 19-72-10054 – nonlinear optics of high-peak-power pulses), and the Welch Foundation (A-1801-20180324).

REFERENCES

[1] P. Eckle, A. N. Pfeiffer, C. Cirelli, A. Staudte, R. Dörner, H. G. Muller, M. Büttiker, and U. Keller, Science **322**, 1525 (2008).

[2] T. Wittmann, B. Horvath, W. Helml, M. G. Schätzel, X. Gu, A. L. Cavalieri, G. G. Paulus and R. Kienberger, Nature Physics **5**, 357 (2009).

[3] A. N. Pfeiffer, C. Cirelli, M. Smolarski, D. Dimitrovski, M. Abu-samha, L. B. Madsen, and U. Keller, Nature Phys. **8**, 76 (2012).

[4] D. Shafir, H. Soifer, B. D. Bruner, M. Dagan, Y. Mairesse, S. Patchkovskii, M. Y. Ivanov, O. Smirnova, and N. Dudovich, Nature **485**, 343 (2012).

[5] A.S. Landsman, M. Weger, J. Maurer, R. Boge, A. Ludwig, S. Heuser, C. Cirelli, L. Gallmann, and U. Keller, Optica **1**, 343 (2014).

[6] E. E. Serebryannikov and A. M. Zheltikov, Optica **3,** 1201 (2016).

[7] A.M. Zheltikov, Phys. Usp. **60**, 1087 (2017).

[8] P. B. Corkum, F. Krausz, Nature Physics **3,** 381 (2007).

[9] A. Couairon, A. Mysyrowicz, Phys. Rep. **441,** 47 (2007).

[10] L. Berge, S. Skupin, R. Nuter, J. Kasparian and J.-P. Wolf, Rep. Prog. Phys. **70,** 1633 (2007).

[11] P.A. Zhokhov and A.M. Zheltikov, Sci. Rep. **8,** 1824 (2018).

[12] L. V. Keldysh, Sov. Phys. JETP **20**, 1307 (1965).

[13] A.M. Perelomov, V.S. Popov, and M.V. Terent'ev, Sov. Phys. JETP **23**, 924 (1966).

[14] G. L. Yudin and M. Yu. Ivanov, Phys. Rev. A **64**, 013409 (2001).

[15] P.A. Zhokhov and A.M. Zheltikov, Phys. Rev. Lett. **113**, 133903 (2014).

[16] P.B. Corkum, Phys. Rev. Lett. **71**, 1994 (1993).

[17] E.E. Serebryannikov and A. M. Zheltikov, Phys. Rev. Lett. **113**, 043901 (2014).

[18] T. Balčiūnas, A. Verhoef, A. Mitrofanov, G. Fan, E. Serebryannikov, M. Ivanov, A. Zheltikov, and A. Baltuška, Chem. Phys. **414**, 92 (2013).

[19] T. Balčiūnas, D. Lorenc, M. Ivanov, O. Smirnova, A. M. Zheltikov, D. Dietze, K. Unterrainer, T. Rathje, G. G. Paulus, A. Baltuška, and S. Haessler, Opt. Express **23**, 15278 (2015).

[20] F. Brunel, J. Opt. Soc. Am. B **7,** 521 (1990).

[21] M. Uiberacker, Th. Uphues, M. Schultze, A. J. Verhoef, V. Yakovlev, M. F. Kling, J. Rauschenberger, N. M. Kabachnik, H. Schröder, M. Lezius, K. L. Kompa, H.-G. Muller, M. J. J. Vrakking, S. Hendel, U. Kleineberg, U. Heinzmann, M. Drescher, and F. Krausz, Nature **446**, 627 (2007).

[22] A.J. Verhoef, A.V. Mitrofanov, E.E. Serebryannikov, D.V. Kartashov, A.M. Zheltikov, and A. Baltuška, Phys. Rev. Lett. **104** 163904 (2010).

[23] A.V. Mitrofanov, A.J. Verhoef, E.E. Serebryannikov, J. Lumeau, L. Glebov, A.M. Zheltikov, and A. Baltuška, Phys. Rev. Lett. **106,** 147401 (2011).

[24] M. Kress, T. Löffler, S. Eden, M. Thomson, and H. G. Roskos, Opt. Lett. **29,** 1120 (2004).

[25] K. Y. Kim, J. H. Glownia, A. J. Taylor and G. Rodriguez, Opt. Express **15,** 4577 (2007).

[26] K.Y. Kim, A.J. Taylor, J.H. Glownia, and G. Rodriguez, Nature Photonics **2,** 605 (2008).

[27] D. J. Cook and R. M. Hochstrasser, Opt. Lett. **25,** 1210 (2000).

[28] J. Dai, X. Xie, and X.-C. Zhang, Phys. Rev. Lett. **97,** 103903 (2006).

[29] T. Bartel, P. Gaal, K. Reimann, M. Woerner, and T. Elsaesser, Opt. Lett. **30,** 2805 (2005).

[30] P.B. Petersen and A. Tokmakoff, Optics Letters **35,** 1962 (2010).

[31] F. Théberge, M. Châteauneuf, G. Roy, P. Mathieu, and J. Dubois, Phys. Rev. A **81,** 033821 (2010).

[32] J.-M. Manceau, A. Averchi, F. Bonaretti, D. Faccio, P. Di Trapani, A. Couairon, and S. Tzortzakis, Opt. Lett. **34,** 2165 (2009).

[33] T. I. Oh, Y. S. You, N. Jhajj, E. W. Rosenthal, H. M. Milchberg and K. Y. Kim, New J. Phys. **15,** 075002 (2013).

[34] Z. Lü, D. Zhang, C. Meng, X. Du, Z. Zhou, Y. Huang, Z. Zhao and J. Yuan, J. Phys. B: At. Mol. Opt. Phys. **46,** 155602 (2013).

[35] M.D. Thomson, V. Blank, and H. G. Roskos, Optics Express **18,** 23173 (2010).

[36] V.□A. Andreeva, O.□G. Kosareva, N.□A. Panov, D.□E. Shipilo, P.□M. Solyankin, M.□N. Esaulkov, P. González de Alaiza Martínez, A.□P. Shkurinov, V.□A. Makarov, L. Bergé, and S.□L. Chin, Phys. Rev. Lett. **116,** 063902 (2016).

[37] C.D. Amico, A. Houard, S. Akturk, Y. Liu, J.Le Bloas, M. Franco, B. Prade, A. Couairon, V.T. Tikhonchuk and A. Mysyrowicz, New J. Phys. **10,** 013015 (2008).

[38] M. Tonouchi, Nature Photonics **1,** 97 (2007).

[39] B. Forestier, A. Houard, M. Durand, Y. B. André, B. Prade, J.-Y. Dauvignac, F. Perret, Ch. Pichot, M. Pellet, and A. Mysyrowicz, Appl. Phys. Lett. **96,** 141111 (2010).

[40] Y. Brelet, A. Houard, G. Point, B. Prade, L. Arantchouk, J. Carbonnel, Y.-B. André, M. Pellet, and A. Mysyrowicz, Appl. Phys. Lett. **101,** 264106 (2012).

[41] M. Châteauneuf, S. Payeur, J. Dubois, and J.-C. Kieffer, Appl. Phys. Lett. **92,** 091104 (2008).

[42] R.R. Musin, M.N. Shneider, A.M. Zheltikov, and R.B. Miles, Appl. Opt. **46,** 5593 (2007).

[43] A. M. Zheltikov, M. N. Shneider, and R. B. Miles, Appl. Phys. B **83,** 149 (2006).

[44] T.S. Rappaport. R.W. Heath, Jr. R. C. Daniels. J. N. Murdock, *Millimeter wave wireless communications* (Prentice Hall, Upper Saddle River, NJ, 2014).

[45] S. Koenig, D. Lopez-Diaz, J. Antes, F. Boes, R. Henneberger, A. Leuther, A. Tessmann, R. Schmogrow, D. Hillerkuss, R. Palmer, T. Zwick, C. Koos, W. Freude, O. Ambacher, J. Leuthold, and I. Kallfass, Nature Photon. **7,** 977 (2013).

[46] A. Motes, *Free-Space Laser Communications: An Introduction* (AM Photonics, 2016).

[47] I. Babushkin, S. Skupin, A. Husakou, C. Köhler, E. Cabrera-Granado, L. Bergé and J. Herrmann, New J. Phys. **13,** 123029 (2011).

[48] O.D. Jefimenko, *Electricity and Magnetism* (Appleton, New York, 1966).

[49] S.A. Akhmanov and S.Yu. Nikitin, *Physical Optics* (Clarendon, Oxford, 1997).

[50] N. B. Delone and V. P. Krainov, Physics–Uspekhi, **41,** 469 (1998).

[51] X. Gao, G. Patwardhan, S. Schrauth, D. Zhu, T. Popmintchev, H.C. Kapteyn, M.M. Murnane, D.A. Romanov, R.J. Levis, and A.L. Gaeta, Phys. Rev. A **95,** 013412 (2017).

[52] K. Schuh, M. Kolesik, E.□M. Wright, J.□V. Moloney, and S.□W. Koch, Phys. Rev. Lett. **118,** 063901 (2017).

[53] Yu.P. Raizer, *Gas Discharge Physics* (Springer, New York, 1991).

[54] P. Sprangle, J. R. Peñano, B. Hafizi, and C. A. Kapetanakos, Phys. Rev. E **69**, 066415 (2004).

[55] *NRL Plasma Formulary*, edited by J. D. Huba, Naval Research Laboratory Publication NRL/PU/6790-98-358 (U.S. GPO, Washington, D.C., 1998).

[56] P. Banks, Planetary Space Sci. **14,** 1085 (1966).

[57] Yu.P. Raizer, Sov. Phys. Usp. **23**, 789 (1980).

[58] G.V. Ostrovskaya and A.N. Zaidel', Sov. Phys. Usp. **16**, 834 (1974).

[59] L. Bergé, S. Skupin, C. Köhler, I. Babushkin, and J. Herrmann, Phys. Rev. Lett. **110,** 073901 (2013).

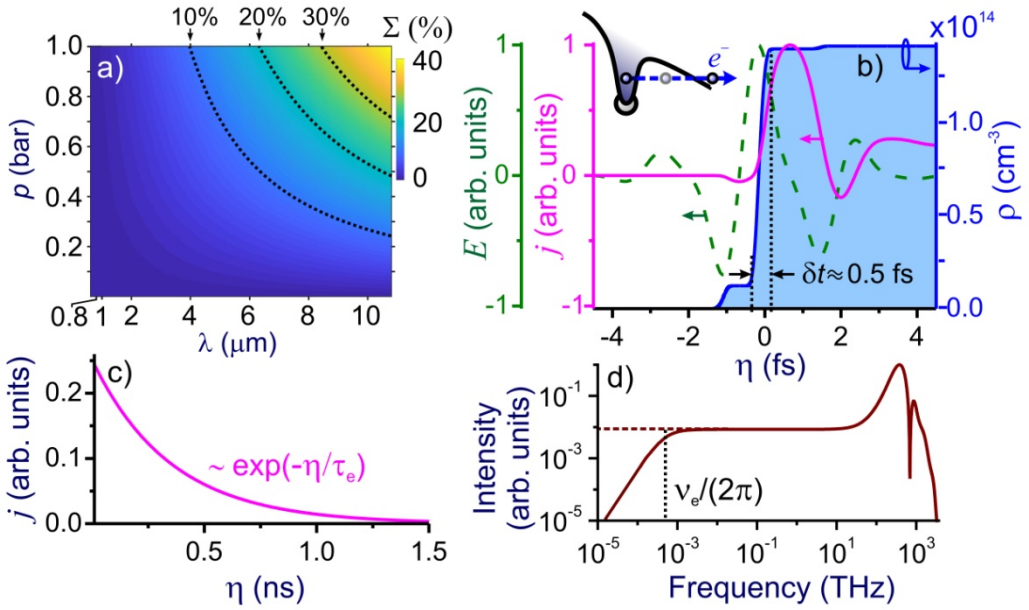

FIG. 1. (a) The ratio Σ as a function of the gas pressure p and the radiation wavelength λ_0 for I_0 = 200 TW/cm^2, $\theta = \pi/2$, and $\xi = 0.3$. (b) Electron density $\rho(\eta)$ (blue line with shading) and tunneling photocurrent $j(\eta)$ (pink line) induced by a two-color field waveform $E(\eta)$ (green line) as defined by Eq. (9) with $\tau_0 = 2.5$ fs, $\xi = 0.3$, $I_0 = 200$ TW/cm^2, and $\theta = \pi/2$ in atmospheric air at $p = 1$ mbar. (c) The dynamics of the photocurrent $j(\eta)$ damped by collisions on a time scale τ_e. (d) The spectrum of multidecade supercontinuum radiated by the photocurrent $j(\eta)$ for $p = 1$ mbar (solid line) and $\nu_e = 0$ (dashed line).

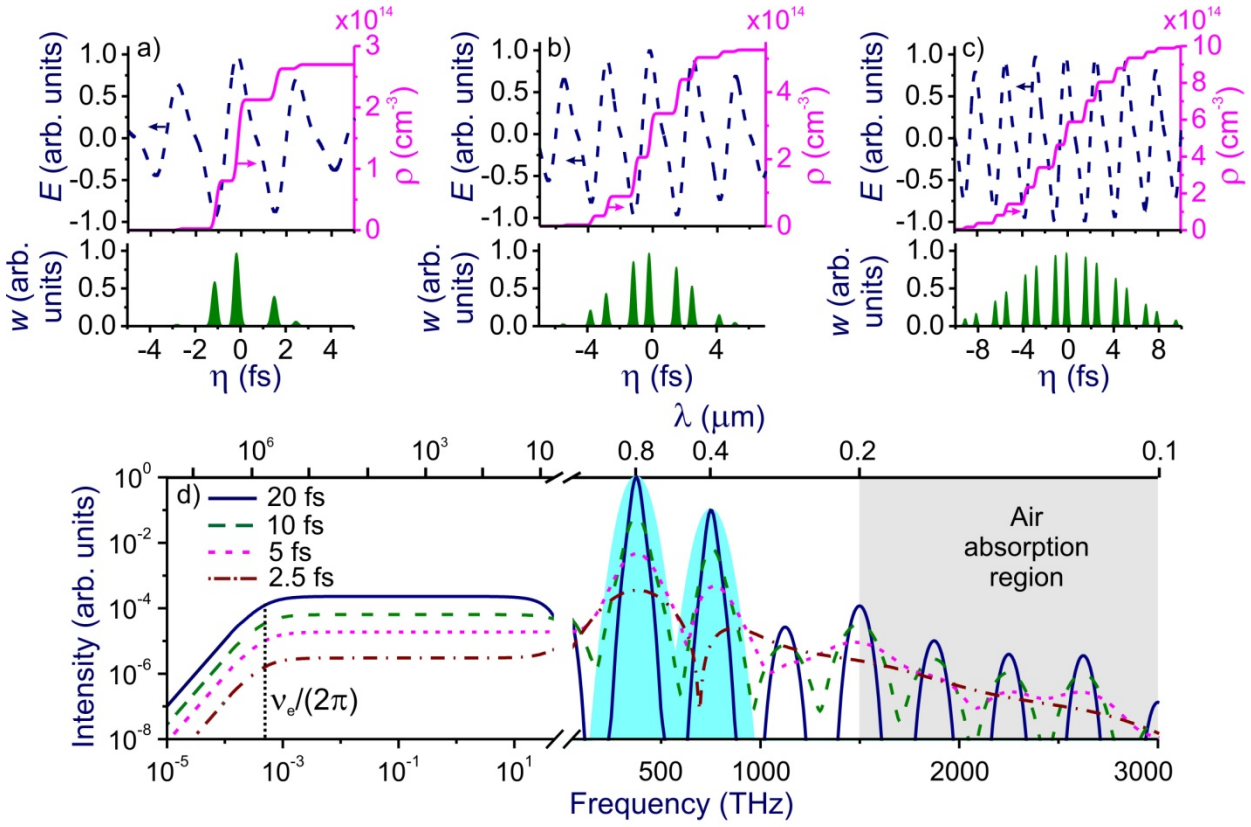

FIG. 2. (a – c) Temporal profiles of the laser field (blue dashed line), ionization rate (green shading), and electron density (pink solid line) in atmospheric air at p = 1 mbar driven by a two-color laser field as defined by Eq. (9) with λ_0 = 800 nm, ξ = 0.3, $\theta = \pi/2$, field intensity I_0 = 200 TW/cm^2, and a pulse width τ_0 = 5 fs (a), 10 fs (b), and 20 fs (c). (d) The spectrum of radiation generated in atmospheric air at p = 1 mbar by a two-color laser driver with λ_0 = 800 nm, ξ = 0.3, I_0 = 200 TW/cm^2, and τ_0 = 20 fs (solid line), τ_0 = 10 fs (dashed line), 5 fs (dotted line), and 2.5 fs (dash–dotted line). The spectrum of the driver with τ_0 = 5 fs is shown by blue shading.

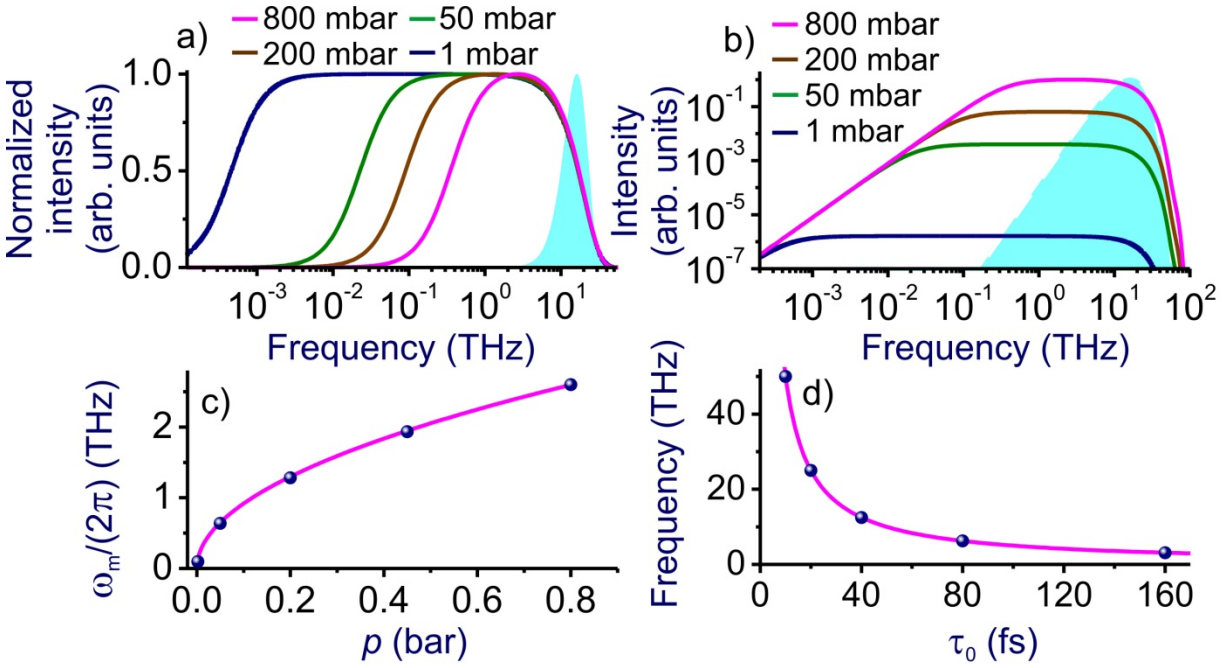

FIG. 3. (a, b) The linear- (a) and log-scale (b) spectra of long-wavelength radiation induced by the tunneling photocurrent in the field of a two-color laser driver (9) with $\lambda_0 = 800$ nm, $\xi = 0.3$, $I_0 = 200$ TW/cm^2, $\theta = \pi/2$, and $\tau_0 = 40$ fs in atmospheric air with a pressure varying from 1 to 800 mbar, as specified in the plot. Also shown is the spectrum of THz radiation generated via two color FWM (blue shading). (c) The frequency ω_m of the maximum in the low-frequency, $\omega/2\pi \leq$ 100 THz part of the supercontinuum spectrum as a function of the gas pressure p: (filled circles) results of simulations and (solid line) $\propto p^{1/2}$ fit. (d) The high-frequency cutoff frequency of the long-wavelength part of the $|E_j(\omega)|^2$ spectrum as a function of the driver pulse width τ_0: (filled circles) results of simulations and (solid line) a $1/\tau_0$ fit.